ROYAL SOCIETY
OF CHEMISTRY

PAPER

Check for updates

A graphene–poly(methacrylic acid)–gold bipyramid hybrid plasmonic nanocomposite for *in vitro* bioimaging and photothermal therapy†

Daria Stoia,[ab] Enza Fazio, [ID][c] Carmelo Corsaro,[c] Andreea Campu,[bd]
Olga Soritau,[e] Ana Maria Craciun, [ID][b] Gabriela Chereches,[e] Monica Focsan, [ID] *[ab]
Giulia Neri [ID] *[f] and Anna Piperno[f]

This study presents two new hybrid nanosystems (G–PMA(1:1)@AuBPs and G–PMA(1:3)@AuBPs), constructed from amine graphene (G-NH$_2$) functionalized with poly(methacrylic acid) (PMA) and gold nanoparticles with a bipyramidal shape (AuBPs). These nanoplatforms behave like efficient photothermal agents, making them suitable for effective *in vitro* photothermal therapy and for bioimaging applications simultaneously. The nanosystems were synthesized by combining covalent and supramolecular approaches and characterized by several techniques including XPS, Raman spectroscopy, UV-vis spectroscopy, XRD, and STEM. It was observed that G–PMA@AuBP systems demonstrate remarkable light-to-heat conversion efficiency under near-infrared irradiation at 785 and 808 nm. Both systems showed an enhancement of the photothermal properties compared to the individual materials. Particularly, a photothermal conversion efficiency exceeding 70% was estimated for the G–PMA(1:3)@AuBP sample under 808 nm irradiation. Beyond their photothermal capabilities, G–PMA@AuBP systems can be effective as label-free bioimaging probes. G–PMA(1:1)@AuBP has been successfully visualized within B16F10 melanoma cells using FLIM, conventional fluorescence, and dark-field microscopy techniques, with localization observed in the perinuclear region. Cytotoxicity assays confirmed the biocompatibility of both nanosystems. Finally, the *in vitro* phototherapeutic efficacy was validated under 808 nm laser irradiation, showing promising results for melanoma cell treatment through photothermal therapy.

[a] *Biomolecular Physics Department, Faculty of Physics, Babes-Bolyai University, 1 M. Kogalniceanu Street, 400084 Cluj-Napoca, Romania.*
E-mail: monica.iosin@ubbcluj.ro

[b] *Nanobiophotonics and Laser Microspectroscopy Center, Interdisciplinary Research Institute in Bio-Nano-Sciences, Babes-Bolyai University, 42 T. Laurian Street, 400271 Cluj-Napoca, Romania*

[c] *Department of Mathematical and Computer Sciences, Physics Science and Earth Science, University of Messina, 31 Viale F. Stagno D'Alcontres, 98166 Messina, Italy*

[d] *Environmental Science, Physics, Physical Education and Sport Department, Faculty of Sciences, Lucian Blaga University, 5-7 Doctor Ion Rațiu Street, 550012 Sibiu, Romania*

[e] *Department of Radiobiology and Tumor Biology, Oncology Institute Prof. Dr Ion Chiricuta, 34-36 Republicii Street, 400015 Cluj-Napoca, Cluj, Romania*

[f] *Department of Chemical, Biological, Pharmaceutical, and Environmental Sciences, University of Messina, 31 Viale F. Stagno D'Alcontres, 98166 Messina, Italy.*
E-mail: giulia.neri@unime.it

† Electronic supplementary information (ESI) available: The equation to compute the photothermal conversion efficiency coefficient (η); absorption spectra of the supernatants for the entrapment efficiency (EE%) calculation; zeta potential measurements of G-NH$_2$, G–PMA(1:1), G–PMA(1:3), and AuBPs; real-time thermal images and heating curves of references (PMA and ultrapure H$_2$O); the MTT assay of G–PMA(1:1)/(1:3) compared to G–PMA(1:1)/(1:3)@AuBP; as well as the control FLIM image of the untreated B16F10 melanoma cells. See DOI: https://doi.org/10.1039/d5tb00097a

Introduction

The scientific community is intensely focused on developing therapeutic nanoagents that are highly effective, biocompatible, and specifically tailored for treating medical conditions. In particular, the development of advanced nanoagents together with specific diagnostic strategies is crucial in the ongoing fight against cancer, a disease projected to cause 13 million deaths by 2030.[1] These nanoagents should also be minimally invasive, exhibit reduced side effects, and be both cost-effective and easily accessible for widespread clinical implementation.

In contrast to traditional cancer treatment methods, photothermal therapy (PTT) emerged as an innovative, safe, efficient, and minimally invasive approach for tumor treatment, using an external laser source to irradiate targeted materials with high photothermal conversion efficiencies.[2–4] PTT uses elevated light powers in the near-infrared (NIR) region to attain subcoagulative (43–55 °C) or coagulative (55–100 °C) temperatures which induce rapid cell death *via* protein denaturation and cell membrane damage.[5,6]

In the wavelength range of 700–1000 nm, known as the "biological transparency window", NIR light demonstrates

superior tissue penetration (from 500 μm to 1–2 cm) compared to light from the visible range (<1 cm), resulting in minimal photodamage to healthy cells and decreased scattering from tissue components.[7] Thus, several materials with strong NIR absorbance are employed for PTT, among these graphene-based nanomaterials (GBNs),[8] carbon nanotubes,[9] and metal or metal oxide nanosystems[10,11] are deeply investigated as photothermal agents (PTAs). However, despite the better photothermal stability and higher photothermal efficiency of these inorganic PTAs, compared to their organic counterparts (polymers, small molecules, etc.), they suffer in terms of biocompatibility and limited functional versatility. To overcome these issues, inorganic–organic nanohybrid PTAs that exhibit advantageous photothermal characteristics including good biocompatibility and enhanced multifunctionality, surpassing the limitations of the individual materials, have been created.[12]

Graphene-based nanomaterials (GBNs) stand out as promising candidates for PTT due to their distinctive structure and unique physico-chemical properties. They exhibit exceptional photothermal conversion ability, at specific wavelengths, including NIR excitation; especially reduced graphene oxide shows an NIR absorbance capacity six times greater than that of graphene oxide, due to a partially restored sp^2 network.[13] Moreover, the large specific surface, together with the high loading capacity and the easy derivatization route, opens the way to GBNs not only in PTT but also in combined therapies due to the combination of photothermal and loading capacities properties.[14] Li et al. developed an efficient drug delivery system (NPF@DOX) based on nanographene oxide nanoparticles and the fluorophore doxorubicin to target the overexposed fibroblast activation protein (FAP) and to perform synergistic chemo-phototherapeutic therapy against oral squamous cell carcinoma.[15] By combining chemotherapy with PTT, NPF@DOX exhibits a high photothermal conversion efficiency (52.48%) under NIR radiation, enhancing localized drug release and apoptosis. FAP-targeted NPF@DOX significantly improves tumor suppression compared to individual therapies, highlighting its potential as a promising strategy for more effective OSCC treatment through synergistic chemophotothermal effects. Although rGO has higher NIR absorption, its low quantum efficiency and broad absorption spectrum render it less sensitive to specific wavelengths. To overcome this limitation and enhance the photothermal effect, an advantageous strategy consists in the derivatization of rGO with gold nanoparticles (AuNPs).[16] The morphological-dependent plasmonic properties of AuNPs allow tuning their absorption wavelength from visible to the NIR region, which holds significant relevance for biomedicine applications,[17] particularly for PTT.[18] AuNPs with bipyramidal shapes (AuBPs), due to their pentagonal base and two sharp apexes, demonstrate appealing optical characteristics, enabling the precise tuning of their localized surface plasmon resonance (LSPR) across the electromagnetic spectrum, especially in the NIR region.[7] Moreover, compared to other Au nanostructures with the same LSPR wavelengths, they can obtain a greater enhancement of both the extinction crosssection and local electric field.[19] They also possess inherent nonradiative properties, rendering them suitable for therapeutic purposes, as they have been proven to effectively convert light energy into heat.[17] A large number of pre-clinical studies provide substantial support for the implementation of PTT for treating various cancers.[20–25] Liu et al. demonstrated the high efficiency of PTT using small-size gold nanobipyramids with strong NIR absorption for liver cancer treatment.[26] With femtosecond laser irradiation, cancer cells are ablated within 20 seconds at just 3 mW power, significantly outperforming control cells, which require higher power and longer exposure. The localized thermal effect leads to rapid temperature rise (516 °C in 106 picoseconds) in a very small area, promoting apoptosis over necrosis, minimizing inflammation, and opening new avenues for minimally invasive photothermal cancer therapy with fewer side effects.

To address these challenges, we developed novel NIR-responsive hybrid nanosystems (G–PMA(1:1)@AuBPs, G–PMA(1:3)@AuBPs), combining for the first time bipyramidal shaped AuNPs with a partially reduced amine graphene (G-NH$_2$), decorated with poly(methacrylic acid) (PMA). The synthesis was performed working at two different G-NH$_2$/PMA weight ratios, 1:1 and 1:3, respectively. The chemical, structural, and morphological features of the as-designed hybrid nanosystems were investigated by several techniques, together with their photothermal capacity. Moreover, the biological properties of G–PMA@AuBPs were evaluated by in vitro experiments on B16F10 cells operating at 808 nm as the light source, while in vitro cell imaging was performed via conventional fluorescence, dark-field microscopy, and fluorescence lifetime imaging (FLIM) techniques. Our results highlight the capability of G–PMA@AuBP systems to act like efficient phototherapeutic, label-free nano scatter, and fluorescent contrast agents against melanoma cancer cells.

Experimental

Materials

Graphene oxide (GO) was purchased from Graphenea (San Sebastian, Spain). (3-Aminopropyl)triethoxysilane (APTES), poly(methacrylic acid, sodium salt) 30 wt% (PMA sodium salt), Dowex 50WX8 hydrogen form, and N-ethyldiisopropylamin 99% (DIPEA) were purchased from Sigma Aldrich. 1-Ethyl-3-(3-dimethyl aminopropyl)carbodiimide hydrochloride (EDC·HCl) and hydroxybenzotriazole (HOBt) were purchased from FluoroChem.

Tetrachloroauric(III) acid trihydrate 99.9% (HAuCl$_4$·4H$_2$O), silver nitrate 99% (AgNO$_3$), cetyltrimethylammonium bromide 99% (CTAB), cetyltrimethylammonium chloride solution 25% in water (CTAC), citric acid (C$_6$H$_8$O$_7$), nitric acid (HNO$_3$), sodium borohydride 99% (NaBH$_4$), and 8-hydroxyquinoline (8-HQL) were purchased from Sigma Aldrich (Missouri, USA).

All the solvents were purchased from Sigma Aldrich. Ultrapure water (MqW) was obtained from the Milli-Q purification system (Merck Millipore) and was used for all aqueous solutions.

The B16F10 melanoma cell line was a gift from Prof. Zahan Marius at the University of Agricultural Sciences and Veterinary Medicine, Faculty of Zootechnics. The reagents used for cell culture studies: MTT [3-(4,5-dimethyl-2-thiazolyl)-2,5-diphenyl-2H-tetrazolium bromide] cell viability reagent, Dulbecco's modified Eagle's medium – high glucose, fetal bovine serum (FBS),

4434 | J. Mater. Chem. B, 2025, 13, 4433–4446

This journal is © The Royal Society of Chemistry 2025

penicillin–streptomycin solution and L-glutamine solution were purchased from Sigma-Aldrich (Missouri, USA).

Synthesis of graphene–poly(methacrylic acid) systems: G–PMA(1:1) and G–PMA(1:3)

GO dispersion of 3.75 mg mL^{-1} in toluene was prepared by sonication treatment for 20 min. Then, 150 μL of APTES was added to partially reduce and to derivatize the GO, and the reaction was refluxed at 70 °C under a nitrogen atmosphere overnight to activate the system.[27] The mixture was centrifuged (4500 rpm, 20 min) and the precipitate underwent sonication-centrifugation cycles using 1:1 MqW:EtOH to remove the unbonded material and finally lyophilized obtaining 140 mg of our amino-graphene nanomaterial (further denoted as G-NH$_2$).

At the same time, 340 mg PMA sodium salt 30% solution was dispersed in 13 mL MqW and treated with Dowex resin. The mixture was stirred for 40 min at room temperature to convert PMA sodium salt into the corresponding acid. The mixture was centrifuged at 5000 rpm for 10 min, then the supernatant was collected and lyophilized.

G–PMA systems were prepared working at two different G-NH$_2$/PMA weight ratios 1:1 and 1:3 respectively. The synthetic strategy to reach the G–PMA(1:1) sample is reported below.

20 mL of G-NH$_2$ water dispersion at the concentration of 5 mg mL^{-1}, were prepared by sonication treatment. In the meantime, 100 mg of PMA was dissolved in 1 mL of MqW, and EDC (20 mg, 0.104 mmol) was added, and the mixture was stirred for 20 min. Then, the G-NH$_2$ dispersion, HOBt (153.14 mg; 0.104 mmol), and DIPEA (10.75 mg; 0.083 mmol) were added and the reaction was left under stirring for 72 h at room temperature. Then, the reaction mixture was centrifugated at 8000 rpm for 30 min. The obtained pellet was resuspended in MqW and sonicated for 20 min, followed by an additional centrifugation for 30 min at 8000 rpm. The washing step was performed for a total of three times. The precipitate was collected and dried in the oven at 35–40 °C for 72 h, obtaining 105 mg of G–PMA(1:1).

Regarding the synthesis of G–PMA(1:3), the G/PMA weight ratio was settled at 1:3, while the amounts of EDC, HOBt, and DIPEA must be considered doubled, compared to the ones previously reported. The experimental conditions remained consistent with those previously reported, resulting in 120 mg of G–PMA(1:3).

Synthesis of colloidal gold nanobipyramids (AuBPs)

The synthesis of highly stable and reproducible nano-bipyramids (AuBPs) was adapted from a previously described seed-mediated growth method.[28] The seeds were prepared by reducing HAuCl$_4$ (0.5 mM) in the presence of CTAC (95 mM), HNO$_3$ (0.25 mM), and NaBH$_4$ solution. Each addition was realized fast under mild stirring at room temperature. The suspension was left for 1 min to eliminate the hydrogen formed through the decomposition of NaBH$_4$. After that, citric acid (1 M) was added and the final solution was left in an oil bath at 85 °C for 1 h 30 min–2 h for the seeds to grow. The synthesized seeds were stored in the dark at room temperature.

The growth solution was prepared by mixing HAuCl$_4$ (25 mM) with CTAB (47 mM), AgNO$_3$ (10 mM), and 8-HQL

(0.4 M in EtOH) under stirring. 40 μL of seeds were added into the reaction and the solution was gently stirred for 10 s, then placed in the oven at 45 °C for 15 min. Then, 25 μL 8-HQL (0.4 M in EtOH) was added to the growth solution and the mixture was left for another 15 min at 45 °C.

Prior to the AuBPs' use, the colloidal nanoparticles were purified through centrifugation at 4500 rpm for 30 min at 25 °C and the precipitate was resuspended in MqW.

A scheme outlining the AuBPs' synthesis is reported in Fig. S1 (ESI†).

Synthesis of graphene–poly(methacrylic acid)–gold bipyramid systems: G–PMA(1:1)@AuBPs and G–PMA(1:3)@AuBPs

For the loading of colloidal AuBPs onto the G–PMA, 50 mg of G–PMA(1:1) or G–PMA(1:3) were dispersed in 8 mL of AuBP colloidal suspension under ultrasonication treatment for 4 h at room temperature. The mixture was then centrifuged at 4500 rpm for 20 min at 25 °C and the precipitate was resuspended in 5 mL of MqW. The washing step was repeated more times and the final precipitate was dried at 35 °C for 48 h. The following samples were produced: G–PMA(1:1)@AuBPs (48 mg) and G–PMA(1:3)@AuBPs (46 mg). The amount of AuBPs loaded onto G–PMA(1:1) and G–PMA(1:3) was estimated by an indirect method, measuring the optical density at the maximum excitation peak of each supernatant. The unloaded AuBPs was ~18% for the G–PMA(1:1)@AuBPs, while for the G–PMA(1:3)@AuBPs the leakage was ~13%. Therefore, the entrapment efficiency percentage (EE%) of the AuBPs was computed to be ~82% for G–PMA(1:1)@AuBPs and ~87% G–PMA(1:1)@AuBPs.

The synthesis method of G–PMA@AuBP nanosystems was schematically illustrated in Fig. 1.

Characterization techniques

The UV-vis-NIR absorption spectra measurements were carried out with a Jasco V-730 UV-vis-NIR spectrophotometer procured from Jasco International Co., Ltd at a spectral resolution of 1 nm. The measurements were performed at room temperature, using quartz glass cuvettes (optical path of 10 mm) from Hellma.

The morphology of the as-developed AuBPs was first analyzed and demonstrated using the transmission electron microscopy (TEM) technique. This technique employs an FEI Tecnai F20 field emission transmission electron microscope operating at an accelerating voltage of 200 kV and equipped with an Eagle 4K CCD camera. The colloidal solution was analyzed by placing a drop (10 μL) of the solution on a carbon copper grid and allowing it to dry at room temperature.

To determine the charge of each hybrid nanosystem's surface, we performed zeta potential measurements using the Zetasizer NanoZS90 equipment from Malvern Panalytical Ltd. A dip cell set (ZEN1002) was used and a 5 V voltage was applied to the samples. All measurements were performed in triplicate.

The morphology of the G–PMA@AuBP hybrid nanosystem was analyzed *via* scanning electron microscopy working in transmission mode (STEM) using a Zeiss-Gemini 2 electron microscope, operating at the accelerating voltage of 30 kV to acquire STEM images. A drop of the suspension was deposited
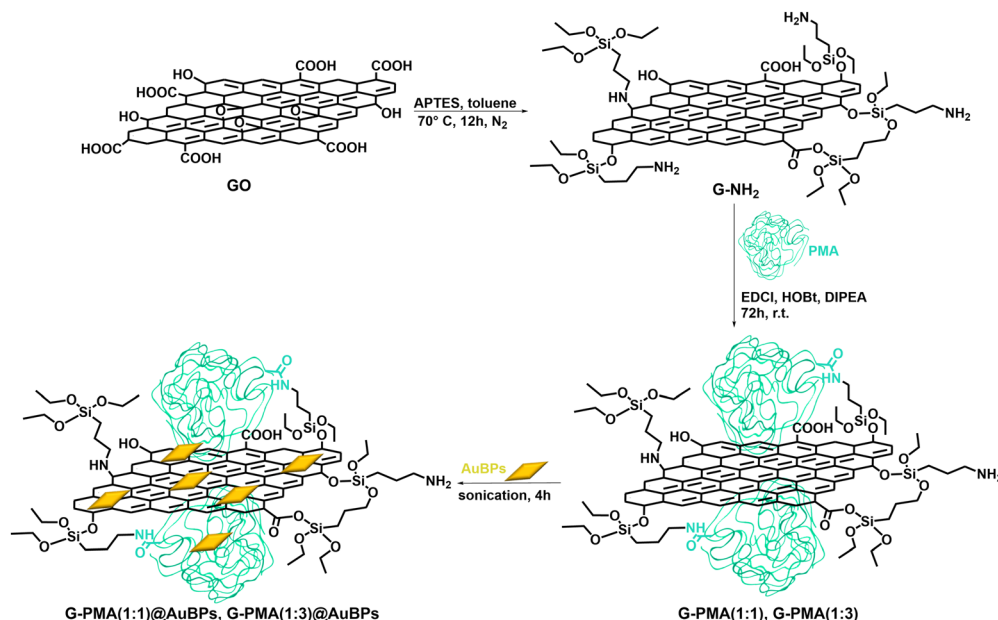
This journal is © The Royal Society of Chemistry 2025

J. Mater. Chem. B, 2025, 13, 4433–4446 | 4435

Fig. 1 Schematic representation of the three-step protocol for the G–PMA@AuBP synthesis: step (1) GO derivatization; step (2) derivatization of G-NH$_2$ with PMA at 1 : 1 and 1 : 3 G-NH$_2$/PMA weight ratio; step (3) anchoring of AuBPs.

on a 400-mesh carbon support sputter-coated with chromium and left to dry at room temperature before analysis.

The surface composition and bonding configurations of the samples were analyzed by means of X-ray photoelectron spectroscopy (XPS). XPS spectra were acquired using the K-alpha system of Thermo Scientific, equipped with a monochromatic Al-Kα source (1486.6 eV), operating in a constant analyzer energy (CAE) mode with a pass energy of 20 eV for high-resolution spectra and a spot size of 400 μm. The advantage software for the K-alpha system was used for the analysis procedure; every core level photoemission peak was deconvoluted with Gauss–Lorentzian shape functions with the same FWHM (1.4 eV) for all of the considered subbands.

The conjugation of PMA onto the G-NH$_2$ surface, as well as the successful loading of AuBPs onto the nanosystem, was analyzed by the micro-Raman spectroscopy using a Horiba XploRa spectrometer equipped with an Olympus BX40 microscope, a Peltier cooled charge-coupled device (CCD) sensor and a 532 nm (2.33 eV) laser as the excitation source. An acquisition time of 80 s allowed a sufficient signal/noise (S/N) ratio.

For additional confirmation of the graphene structure as well as the successful loading of AuBPs onto the nanosystem, X-ray diffraction (XRD) measurements were performed. XRD spectra were obtained by using a Shimatzu XRD-6000 diffractometer with a graphite monochromator. All measurements were performed at room temperature, in the 2θ range between 5 and 90 degrees. The samples were mildly pre-grounded in an agate mortar in order to minimize the preferred orientation, which created a systemic error in the observed diffraction peak intensities.

Photothermal effects

For the photothermal performance evaluation of the G–PMA@AuBP nanosystem, we tested the photoactive agent's potential to efficiently generate heat in solution after exposing it to two different NIR laser excitations, specifically 785 and 808 nm. 500 μL of each hybrid nanosystem (1 mg mL^{-1}) – G–PMA(1 : 1)@AuBPs and G–PMA(1 : 3)@AuBPs – were exposed for 15 min continuously to both excitation wavelengths, while real-time thermal images were acquired every 30 s during the irradiation, using an IR thermographic camera (Optris PI 450, Remscheid, Germany). Moreover, the IR thermographic camera acquired real-time thermal images every 30 s during the cooling step of each sample. All experiments were performed at room temperature. Moreover, as control samples, we irradiated and analyzed colloidal AuBPs, G-NH$_2$, PMA, and ultrapure H$_2$O. Based on the real-time thermographic images that we acquired, we extracted the temperature difference with respect to the initial temperature of the sample to further calculate the cooling time constant and, finally, the photothermal conversion efficiency (η) for the G–PMA(1 : 1)@AuBPs and G–PMA(1 : 3)@AuBPs exposed to both lasers using an analytical method,[29] as explained in the ESI.†

Cell viability

The viability of the B16F10 melanoma cells in the presence of different amounts of G–PMA(1 : 1)@AuBPs and G–PMA(1 : 3)@AuBPs (from 0 to 40 μL of G–PMA@AuBP dispersion 0.3 mg mL^{-1} in PBS) was evaluated. The cells were cultivated under standard conditions in Dulbecco's modified Eagle's medium (high glucose with 10% FBS), 1% antibiotics (penicillin and streptomycin), and 2 mM L-glutamine at 37 °C in an incubator with 95% humidity. B16F10 melanoma cells were seeded in 96-well plates (Thermo Fischer Scientific) at a concentration of 10^4 cells per well in a 200 μl medium. After 24 h, having attached the cells to the plate, treatments with nanoparticles were performed. The cell viability was evaluated after 24 h post-treatment when the culture medium was discarded from the 96-well plates and 100 μl per well of

4436 | *J. Mater. Chem. B*, 2025, **13**, 4433–4446

This journal is © The Royal Society of Chemistry 2025

1% MTT solution was added. The plates were incubated for 1 h at 37 °C in the dark. The MTT solution was removed and 150 μl of DMSO/well was added. Each probe was analyzed in triplicate. The plate reading was performed with a BioTek Synergy 2 microplate reader (Winooski, VT, USA) at a wavelength of 570 nm. MTT (3-(4, 5-dimethylthiazolyl-2)-2,5-diphenyltetrazolium bromide) is a tetrazolium salt that is converted by mitochondrial reductases in viable cells into dark blue formazan crystals. The results obtained as optical density values were calculated as percentages relative to the 100% value of the controls.

In vitro imaging

Dark-field and conventional fluorescence cell images were captured with an Axio Observer Z1 Inverted Microscope from Carl Zeiss, utilizing an AxioCam MRn monochrome microscope camera, and processed via ZEN software. Fluorescence excitation was achieved using an HXP 120 °C mercury lamp, with image acquisition performed through a 20× objective (Zeiss, LD Plan-Neofluar, NA = 0.4), equipped with a high numerical dark-field immersion condenser (Achromatic-Aplanatic, NA = 1.4, Zeiss). For the nuclei visualization (stained with DAPI), the light was reflected by a dichroic mirror using a G 365 excitation filter (Zeiss G 365), a BP 445/50 band emission filter, and a 395 nm long pass dichroic mirror (Zeiss FT 395).

Confocal FLIM assays were conducted on the B16F10 melanoma cells treated with G–PMA(1:1)@AuBPs. These measurements were performed with a MicroTime200 time-resolved confocal fluorescence microscope system (PicoQuant, Berlin, Germany) equipped with an Olympus IX 71 microscope. The FLIM images were obtained under the excitation wavelength of 520 nm (diode laser LDH-D-C-510, 1.1 μW, 40 MHz, PicoQuant) using a PLAN N40X/N.A. = 0.65 objective and a FF01-519LP emission filter (Semrock). The signal collected through the objective was filtered spectrally and spatially using a pinhole (50 μm) and then directed onto a PDM single photon avalanche diode from MPD. Subsequently, the data were processed by the data acquisition unit (PicoHarp 300 time-correlated single photon counting (TCSPC)). The microscope is equipped with a piezo x–y scanning table and a PiFocz-piezo actuator to facilitate imaging assays.

In vitro irradiation

The real-time phototherapeutic effect of the G–PMA(1:1)@AuBP and G–PMA(1:3)@AuBP hybrid nanosystems on B16F10 melanoma cells was studied. The cells were seeded in 96-well plates and treated for 24 h with the two nanosystems. Following the treatment, the medium was changed with PBS and the cells were exposed to the 808 nm laser for 15 min, using the same experimental conditions as the in-solution studies. The control samples, B16F10 cells treated with the hybrid nanosystem but without the NIR laser irradiation, were kept at room temperature during the irradiation of the cells treated and exposed to NIR light, to match the conditions of the treated samples. The cell viability was evaluated after 24 h post-irradiation using an MTT colorimetric assay, as described before. Statistical differences were analyzed for each nano-system treatment compared to the irradiated control respectively non-irradiated cells with the repeated measures ANOVA test followed by Dunnett's multiple comparison test with the setting of p-value < 0.05 regarded as significant. The comparison between irradiated vs. non-irradiated cells was performed with two-way ANOVA analysis. The significances were thus noted in the graphical representations: ns $p > 0.05$, $*p < 0.05$, $**p < 0.01$ or $***p < 0.001$.

Results and discussion

Design and characterization of the hybrid nanosystems (G–PMA(1:1)@AuBPs, G–PMA(1:3)@AuBPs)

The G–PMA@AuBP nanoplatforms were prepared by a three-step procedure using a covalent approach for the organic functionalization of the graphene surface, whereas AuBPs were entrapped by a non-covalent approach, as schematically illustrated in Fig. 1.

In our study, G-NH$_2$ was selected to reach a carbon-based nanomaterial characterized by high NIR absorption capacity, compared to graphene oxide, and also fluorescence responsivity to act as a contrast agent[30] for in vitro cell tracking. In particular, it was synthesized by treating commercial GO with APTES, through a concurrent reduction and derivatization process.[27]

To improve the biocompatibility and colloidal stability of the obtained graphene derivative, G-NH$_2$ was covalently derivatized with PMA, a water-soluble and biocompatible synthetic polyanion used as a capping agent towards metal clusters.[31] The coupling reaction was performed at two different G:PMA weight ratios (i.e., 1:1 and 1:3) obtaining G–PMA(1:1) and G–PMA(1:3), respectively. Subsequently, AuBPs were loaded onto the G–PMA(1:1) or G–PMA(1:3) matrix via electrostatic interactions, reaching two hybrid nanosystems G–PMA(1:1)@AuBPs and G–PMA(1:3)@AuBPs, respectively (Fig. 1).

AuBPs were prepared by the seed-mediated growth method (Fig. S1, ESI†), which consists of two main steps: (i) the synthesis of the seeds, and (ii) their growth as anisotropic nanoparticles.[28] Parameters such as seed structure, used surfactants, metal ions interaction, and growth kinetics strongly affect the synthetic process. Particularly, the gold seeds were kept at 85 °C to promote their formation as a polycrystalline structure[28,32] and favor the subsequent growth as bipyramidal structures. The anisotropic growth with elongated morphology is also favored by the presence of silver ions (Ag$^+$)[33-35] and helped by surfactant agents such as CTAB and CTAC.[28]

The obtained AuBPs are thoroughly characterized both optically and morphologically. As seen in Fig. 2A, the extinction spectrum exhibits the AuBPs' characteristic LSPR response, showing two distinct peaks: (i) an LSPR peak around 520 nm, corresponding to transversal oscillations of conduction electrons at the metallic surface; and (ii) a narrower and more intense peak at 803 nm, resulting from the oscillations along the longitudinal axis. In fact, the AuBPs were intentionally synthesized to exhibit a longitudinal LSPR response at 803 nm due to previous findings of our group,[29] which demonstrated the AuBPs with LSPR responses near the resonance condition of selected laser excitation wavelengths (785 and 808 nm) offer the

This journal is © The Royal Society of Chemistry 2025

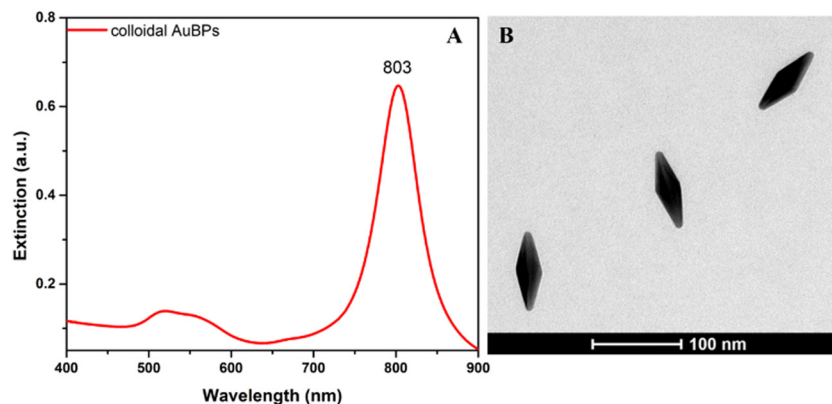J. Mater. Chem. B, 2025, **13**, 4433–4446 | **4437**

Fig. 2 (A) Extinction spectrum of colloidal AuBP solution. (B) TEM image of AuBPs.

best light-to-heat conversion performances, making them efficient thermoplasmonic nanogenerators and ideal agents for PTT applications.

No changes in the extinction profile of AuBPs are observed after one week of storage (Fig. S2, ESI†).

The morphology of AuBPs was investigated by the TEM technique (Fig. 2B), resulting in an aspect ratio of 4.6. The AuBPs were intentionally synthesized to exhibit a longitudinal LSPR response at 803 nm due to previous findings of our group,[29] which demonstrated that AuBPs with LSPR responses near the resonance condition of selected laser excitation wavelengths (785 and 808 nm) offer the best light-to-heat conversion performances, making them efficient thermoplasmonic nanogenerators

and ideal agents for PTT applications. Furthermore, zeta potential measurements indicate the positive potential of AuBPs (7.62 ± 0.98 mV), which makes them suitable for subsequent grafting on the negatively charged G–PMA sheets (Table S1, ESI†).

The successful loading of AuBPs onto the G–PMA platform was provided by STEM-EDX measurements. First, G–PMA layers are characterized by homogeneous, quite smooth, and transparent sheets, with little aggregation. The presence of well-defined edges revealed many thin sheets of graphene, with ripple lines between the layers, as seen in Fig. 3A and C. G–PMA(1 : 1)@AuBPs and G–PMA (1 : 3)@AuBPs are shown in Fig. 3B and D. AuBPs are mainly distributed on the edges of the graphene layers, with a higher amount of AuBPs loaded onto G–PMA(1 : 3) (Fig. 3D).
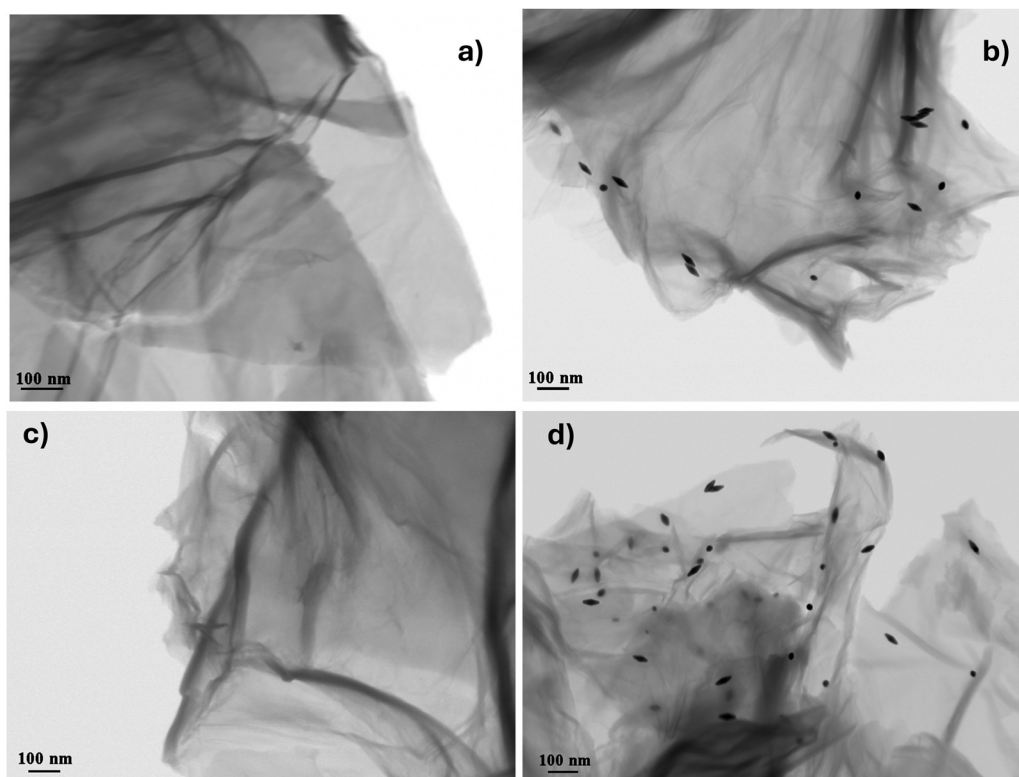

Fig. 3 Representative STEM images: (a) G–PMA(1 : 1); (b) G–PMA(1 : 1)@AuBPs; (c) G–PMA(1 : 3); (d) G–PMA(1 : 3)@AuBPs.

The amount of Au loaded on G–PMA(1:3)@AuBPs and G–PMA-(1:1)@AuBPs, estimated by EDX elemental analysis (Table S2, ESI†), is of 1.12% and 0.45% respectively.

The surface charge of the obtained G–PMA@AuBP hybrid nanosystems has been measured to be −22.7 ± 1.42 mV for G–PMA(1:1)@AuBPs and −9.51 ± 1.41 mV for G–PMA(1:3)@AuBPs. These values are considerable higher in comparison with ones evaluated for the starting materials (Table S1, ESI†). Thus, zeta potential modification can be assigned to the grafting of the positively charged AuBPs on G–PMA systems.

UV-vis absorption spectroscopy indirectly evaluated the entrapment efficiency percentage (EE%) of the AuBPs on both the G–PMA matrixes. The absorption spectra of the supernatant arising from the washing cycles performed on G–PMA(1:1)@AuBPs and G–PMA(1:3)@AuBPs were compared to the one of the colloidal AuBPs (Fig. S3, ESI†). EE was higher than 80% on both considered samples, and no further AuBP leakage after the second washing cycle was observed.

The surface functionalization of G-based materials was also investigated through XPS analysis. As expected, in G-NH₂, the amount of carbon and oxygen, estimated by the survey spectra, decreases with respect to GO, together with the appearance of

both nitrogen and silicon content at around 9% and 10%, respectively. The experimental data are in agreement with the simultaneous reduction and derivatization process performed by APTES (see Table 1). After PMA grafting the carbon and oxygen content percentages remain almost unchanged in the G–PMA(1:1) compound, whereas an increase of ∼2% was observed in the PMA(1:3) sample (see Table 1). XPS features typical of Au species are not detected because their content is certainly below the XPS detectability threshold.

To further investigate the surface bonding configurations, we deconvoluted high-resolution XPS spectra. C 1s bands were deconvolved using six contributions: a main contribution at 284.5 eV attributed to C=C/C–C in the aromatic ring and four other contributions at higher binding energies corresponding to carbon atoms bonded to oxygen in different surface functionalities (C–OH, C–N, C–O–C and C=O) centered at 285.0, 285.8, 286.9, and 288.0 eV, respectively (Fig. 4). The contribution at about 290.0 eV refers to π–π bonds. Table 2 reports the percentage of the different contributions to the whole band.

Going from the G-NH₂ sample to G–PMA@AuBP ones, we have observed a decrease of C=C/C–C bonding configurations, while C–OH and C–N percentages increase, as estimated by the fitting profiles shown in Fig. 4; then all the other carbon-oxide phases remain almost unchanged. Moreover, N 1s lineshapes (Fig. S4, ESI†) show a similar profile in all the samples and are characterized by three peaks at about 399, 400, and 401.5 eV, representative of the formation of SiN_xO_y, N–C functionality, and N–O/alkyl ammonium $(NR_4)^+$ groups, respectively (see Table S3, ESI†).

To study the disorder and defect levels of G-NH₂ and to confirm the successful development of G–PMA@AuBP hybrid nanosystems, micro-Raman spectroscopy was employed. Generally, the Raman

Table 1 Sample composition estimated by deconvolving XPS survey spectra

Samples	C (%)	O (%)	N (%)	Si (%)
GO	67.01	32.99	—	—
G-NH₂	56.26	24.46	8.86	10.42
G–PMA(1:1)	56.25	24.93	9.78	9.04
G–PMA(1:3)	58.07	26.37	7.07	8.49
G–PMA(1:1)@AuBPs	61.92	24.59	7.74	5.75
G–PMA(1:3)@AuBPs	59.08	25.08	8.21	7.63

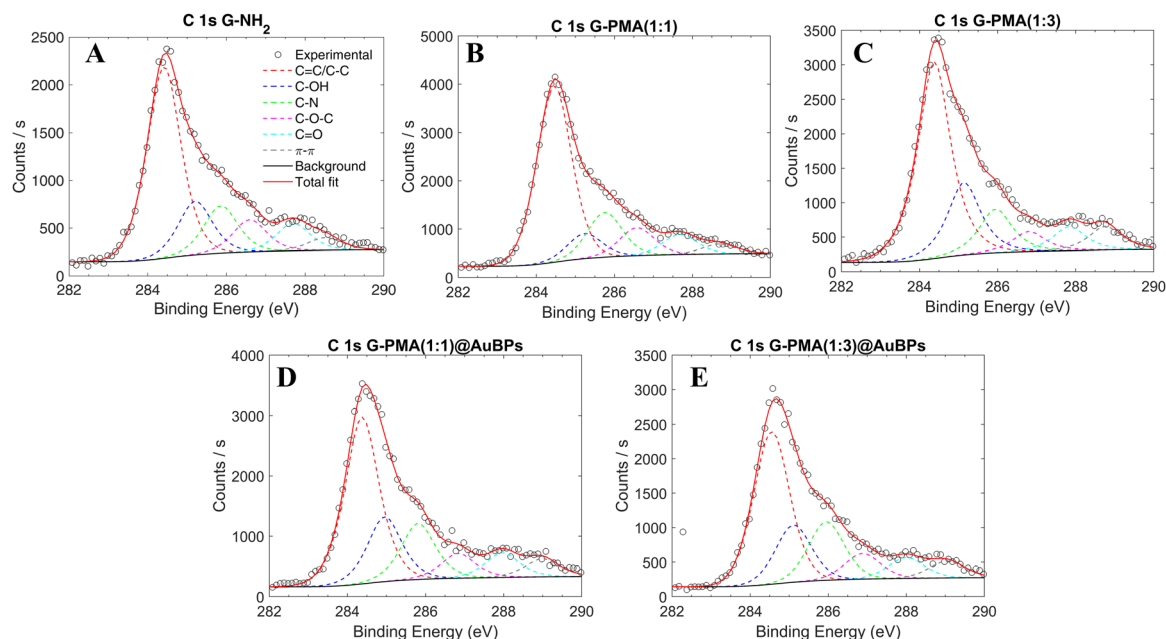**Fig. 4** High-resolution C 1s deconvoluted spectra of (A) G-NH₂, (B) G–PMA(1:1), (C) G–PMA(1:3), (D) G–PMA(1:1)@AuBPs, and (E) G–PMA(1:3)@AuBPs.

This journal is © The Royal Society of Chemistry 2025

J. Mater. Chem. B, 2025, **13**, 4433–4446 | **4439**

spectrum of graphite exhibits the G band at 1580 cm^{-1} and the D band at 1350 cm^{-1}.[36] The G band is due to the first-order scattering of the E_{2g} mode, whereas the D band is related to the defect in the graphite lattice.[36] The Raman spectrum of G-NH$_2$ (black spectrum) is presented in Fig. 5A, together with the Raman spectrum of G–PMA (blue spectrum), G–PMA(1:1)@AuBPs (red spectrum), and G–PMA(1:3)@AuBPs (green spectrum). As observed in Fig. 5A, all the investigated samples exhibit the presence of the G band at 1660 cm^{-1} and the D band at 1380 cm^{-1}. The shift of these bands towards a higher wavenumber, together with the broadening of the D band in the G-based nanomaterial is associated with the oxidation of graphite and the size reduction of the in-plane sp^2 domains during the oxidation.[37] The G* band (a combination of a transverse optical and longitudinal acoustic phonon mode near the K-point, resulting from double resonance Raman scattering processes) appears in the 2400–2450 cm^{-1} region of the spectra, while the not well-defined second-order overtone 2D mode is centered at about 2690 cm^{-1}.[38]

Using the I_D/I_G peak intensities ratio, we characterized the level of disorder for the analyzed samples. For all the samples, this value is lower than 0.5, indicating that the functionalization with APTES had a limited effect on the pristine graphene structure; only after adding PMA (blue spectrum), the specific G, D, and 2D bands are not well defined, since PMA successfully covers the graphene. As expected, after loading the AuBPs, the Raman signal of the graphene lattice (red and green spectrum) is enhanced, and the

surface-enhanced Raman spectroscopy (SERS) effect takes place.[39] Moreover, the increase and the shrinkage of all the detected Raman features after the loading of the AuBPs, suggest the tight anchoring of Au nanostructures on the G–PMA platforms, thus generating a large number of "hot spots". This is additional direct proof of the successful loading of AuBPs onto G–PMA nanosystems.

To demonstrate the crystallinity of the G–PMA nanosystems, as well as the successful loading of AuBPs onto the G–PMA(1:1) and G–PMA(1:3), the XRD technique was implemented. Corresponding XRD patterns of both graphene and AuBPs are presented in Fig. 5B. The specific graphene diffraction lines of the G-NH$_2$ sample – G(002) and G(100) – can be easily identified in the black spectrum. The G(002) peak located at 2θ = 23.2 can be correlated with the interlayer spacing between the graphitic layers.[40] Note that, after PMA grafting, the G-NH$_2$ crystallinity is preserved (blue spectrum).

The four characteristic Au diffraction peaks can be identified at 38.1, 44.3, 64.5, and 77.7 degrees in both G–PMA(1:1)@AuBPs and G–PMA(1:3)@AuBP samples. All four peaks – (111), (200), (220), and (311) – are in agreement with the standard Bragg reflection of the face center cubic lattice. The intense diffraction peak at 38.1 suggests that the preferred growth orientation of zero-valent gold was fixed in the (111) direction.[41] Moreover, the intensity of the (111) reflection peak depends on the amount of Au in the sample. Consequently, we have further validation that the G–PMA(1:3) nanosystem can accommodate a larger quantity of AuBPs on its surface, attributable to the increased presence of PMA, which enhances the loading capacity of G–PMA in relation to its capping agent properties towards metal clusters.

Light-to-heat conversion efficiency of the G–PMA@AuBP hybrid nanosystems

The ability of the G–PMA@AuBP nanosystems to behave as efficient PTAs when exposed to NIR laser radiation was first assessed in a liquid environment. Specifically, G–PMA(1:1)@AuBPs and G–PMA(1:3)@AuBPs, along with G-NH$_2$, PMA, G–PMA(1:1), G–PMA(1:3), and colloidal AuBP control solutions
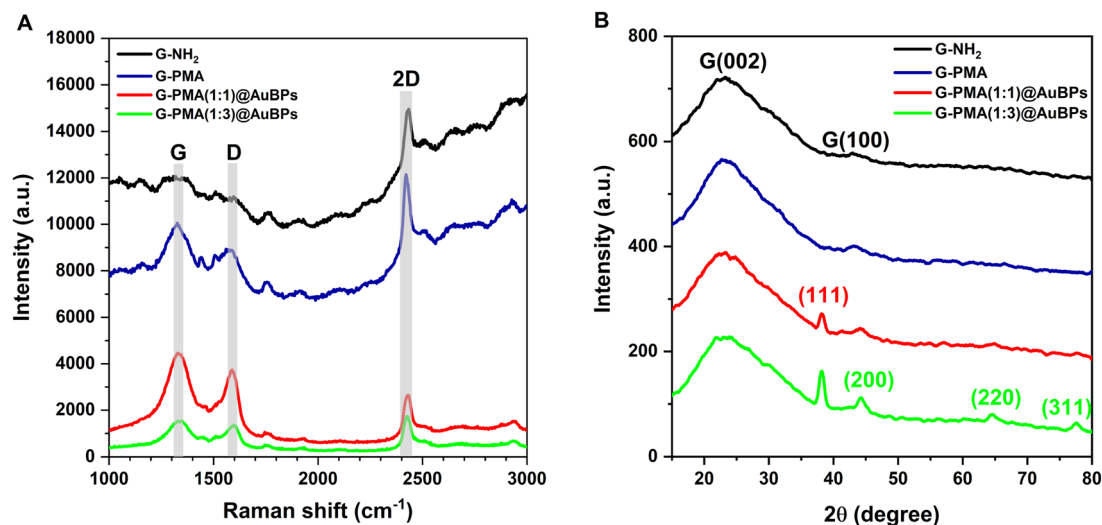
Table 2 Percentage of the different contributions to the C 1s XPS band

Samples	C=C/ C–C (%)	C–OH (%)	C–N (%)	C–O–C (%)	C=O (%)	π–π (%)
G-NH$_2$	52.59	14.70	12.97	8.81	7.50	3.42
G–PMA(1:1)	58.04	8.20	14.75	9.17	6.57	3.27
G–PMA(1:3)	51.73	19.05	11.47	5.25	6.33	6.17
G–PMA(1:1)@AuBPs	47.03	18.25	15.79	6.95	6.89	5.08
G–PMA(1:3)@AuBPs	46.12	17.22	17.63	7.70	6.26	5.06

Fig. 5 (A) Raman spectra of G-NH$_2$ (black) and G–PMA (blue), G–PMA(1:1)@AuBPs (red), and G–PMA(1:3)@AuBPs (green) in the 1000–3000 cm^{-1} region. (B) XRD analysis of G-NH$_2$ (black), G–PMA (blue), G–PMA(1:1)@AuBPs (red), and G–PMA(1:3)@AuBPs (green).

4440 | *J. Mater. Chem. B*, 2025, **13**, 4433–4446

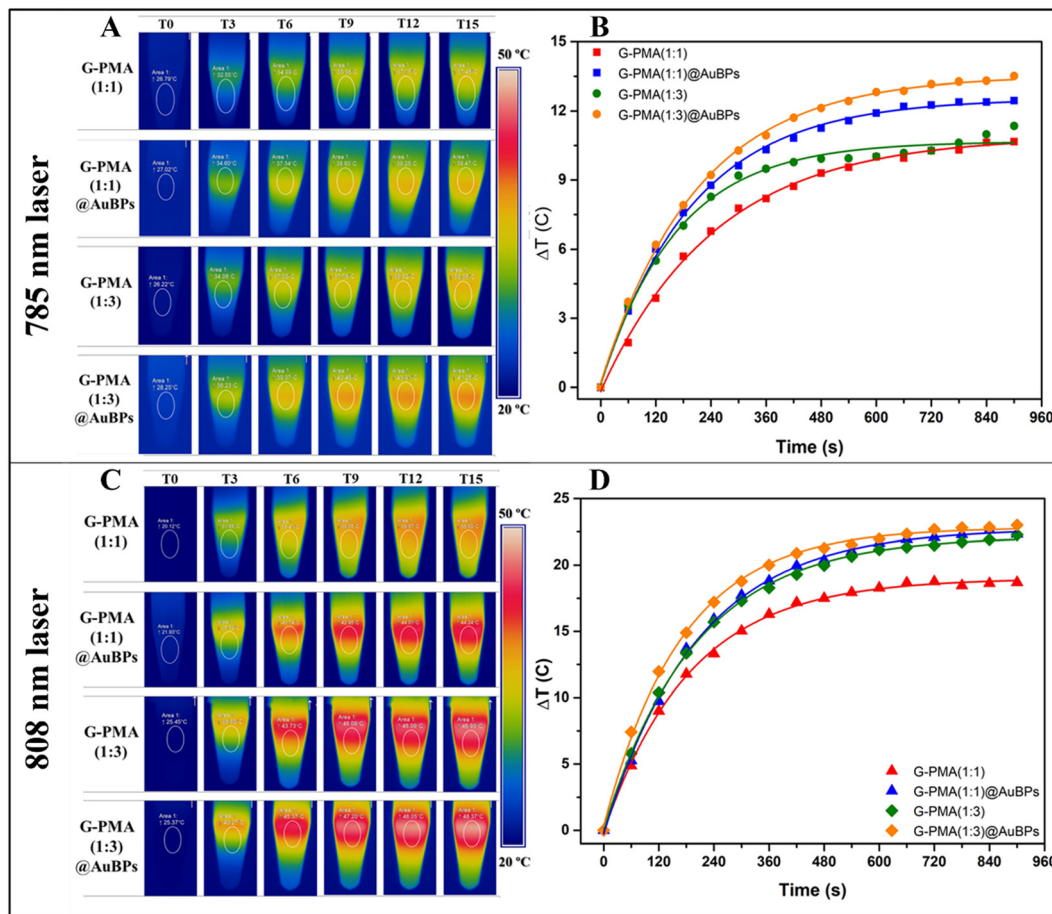This journal is © The Royal Society of Chemistry 2025

Fig. 6 Photothermal performance of G–PMA@AuBP nanosystems under 785 and 808 nm laser irradiation. (A) and (C) Real-time thermal images of G–PMA(1 : 1), G–PMA(1 : 1)@AuBPs, G–PMA(1 : 3), and G–PMA(1 : 3)@AuBP solutions captured during 785 nm and 808 nm laser irradiation at 0, 3, 6, 9, 12, and 15 minutes. (B) and (D) Temperature differences (ΔT) plotted over time, showing enhanced heating for AuBP-functionalized hybrid nanosystems. The nanosystems exhibit greater ΔT under 808 nm irradiation, highlighting wavelength and composition-dependent photothermal performance.

were subjected to irradiation by two different NIR lasers, operating at 785 and 808 nm. Fig. 6A, C, Fig. S5A, and S6 (ESI†) show the real-time thermal images recorded from the beginning (T_0) and subsequently, every 3 minutes throughout the irradiation process using the 785 nm and, alternately, the 808 nm lasers, with both lasers being in resonance with the plasmonic AuBPs.

The thermal images are analyzed to extract temperatures at an interval of 1 min during irradiation, allowing computation of the temperature difference (ΔT) in relation to the initial ambient temperature. These ΔT values are then plotted against the duration of the irradiation, yielding the thermal curves (Fig. 6B and D). When the nanosystems were exposed to the 785 nm laser, G–PMA(1 : 1) reached a maximum temperature difference of 11 °C, similar to the one of G–PMA(1 : 3) (12 °C), while G–PMA(1 : 1)@AuBPs and G–PMA(1 : 3)@AuBPs showed slightly higher ΔT peaks, respectively of 13 and 14 °C (see Fig. 6B). When the systems were exposed to irradiation at a laser wavelength of 808 nm under identical parameters, the G–PMA(1 : 1) reached a ΔT of 19 °C, whereas G–PMA(1 : 3) attained a ΔT peak of 22 °C. In contrast, G–PMA(1 : 1)@AuBPs exhibited a ΔT peak of 23 °C, and G–PMA(1 : 3)@AuBPs recorded a peak of 24 °C (refer to Fig. 6D). These results indicate that all

Table 3 ΔT_{max} of each sample irradiated with the two NIR lasers, 785 and 808 nm, during a 15 min period

Samples	ΔT_{max} (785 nm)	ΔT_{max} (808 nm)
G–PMA(1 : 1)	11 °C	19 °C
G–PMA(1 : 1)@AuBPs	13 °C	23 °C
G–PMA(1 : 3)	12 °C	22 °C
G–PMA(1 : 3)@AuBPs	14 °C	24 °C

nanosystems exhibit superior photothermal performances under 808 nm laser irradiation. It is important to note that the temperature increase depends on the specific laser utilized and the nanosystem being examined.

To sum up, all ΔT_{max} values are compiled in Table 3.

In parallel, we also analyzed the behavior of the individual G-NH$_2$ and colloidal AuBPs used as control samples when exposed to the same two laser lines. As presented in Fig. S5 (ESI†), the two samples are able to convert light-to-heat when exposed to the two NIR lasers, G-NH$_2$ with a ΔT_{max} value of 8.32 °C when exposed to a 785 nm laser, and a ΔT_{max} of 12.9 °C when exposed to the 808 nm laser. Colloidal AuBPs exhibit the same behavior, with a ΔT_{max} of 11.34 °C at 785 nm laser exposure

This journal is © The Royal Society of Chemistry 2025

J. Mater. Chem. B, 2025, **13**, 4433–4446 | **4441**

and a ΔT_{max} of 12.42 °C at the 808 nm laser irradiation. Moreover, we confirmed and demonstrated that even though both samples – G-NH$_2$ and AuBPs – are efficient PTAs, their combination resulted in a plasmonic nanocomposite with significantly enhanced photothermal ability.

Concerning free PMA and the MqW control solutions, they do not exhibit photothermal activity with respect to the wavelength of excitation. The real-time thermal images of the two control samples, exposed to both NIR lasers, are presented in Fig. S6 (ESI†).

It is widely known that tumor cells exhibit greater sensitivity to temperature elevation compared to normal healthy cells.[42] Currently, temperatures ranging between 42 and 43 °C are deemed fatal for tumor cells. The diminished heat dissipation due to impaired blood flow in tumors, in contrast to normal tissues, aids in thermal containment, thereby intensifying the detrimental impact.[43] Moreover, existing literature underscores the importance of maintaining precise control over tissue temperature, ensuring it remains within the range of 40 to 60 °C.[44] Temperatures exceeding 60 °C can trigger protein denaturation, resulting in decreased viability. In our case, the recorded T_{max} of G–PMA(1:1)@AuBPs was 39 °C and of G–PMA(1:3)@AuBPs was 40 °C when exposed to a 785 nm laser, while T_{max} was 45 °C and 48 °C for G–PMA(1:1)@AuBPs and G–PMA(1:3)@AuBPs respectively when exposed to a 808 nm laser. Although the temperature reached by G–PMA@AuBPs in solution is localized within the aforementioned range, it is crucial to note that this temperature is determined for the entire irradiated volume. The efficacy of the photothermal effect is heavily influenced by NP concentration and laser exposure duration.[29] Given that cells internalize a notably lower concentration of the as-developed hybrid nanosystems, prolonged exposure is necessary to reach peak temperature.[45] Additionally, the 785 nm laser line induced a T_{max} of ~39 °C in solution, close to the low limit of the range, indicating the significant role of the irradiation source in temperature regulation. Thus, manipulation of the different parameters allows precise control over temperature, ensuring the desired therapeutic effects without introducing significant additional impacts.

The photothermal conversion efficiency coefficient (η) of the hybrid nanosystem was calculated using an energy balance equation that considers both the laser energy input (Q_{laser}) and the energy loss (Q_{loss}) during the heating process. Q_{laser} is determined by the absorbed light from both the hybrid nanosystem and the solvent, accounting for the incident laser power and absorption characteristics. The heat transfer coefficient (h) and the irradiated surface area (A) were used to calculate Q_{loss}. The product of h and A was extracted using the time constant (τ_s), which was obtained from the slope of the cooling curve, described by temperature driving force (θ). This approach allows for the determination of η for the different hybrid nanosystems under 785 and 808 nm laser irradiation. Making use of eqn (1) we determined analytically the η for the G-NH$_2$, colloidal AuBPs, G–PMA(1:1)/(1:3), and the G–PMA(1:1)/(1:3)@AuBPs.

$$\eta = \frac{h \times A\Delta T - I\xi}{I(1-\xi)(1-10^{-A_\lambda})} \quad (1)$$

Table 4 The calculated photothermal conversion efficiency coefficient (η) of all the samples, for both NIR laser lines

Sample	η (785 nm)	η (808 nm)
G-NH$_2$	41%	34%
AuBPs	74%	43%
G–PMA(1:1)	60%	66%
G–PMA(1:1)@AuBPs	62%	71%
G–PMA(1:3)	65%	81%
G–PMA(1:3)@AuBPs	75%	75%

where h is the heat transfer coefficient, A is the laser exposed surface area cross-section, ΔT is the temperature difference with regard to the ambient temperature, I is the incident laser power, ξ is the energy fraction absorbed by the Eppendorf and solvent, and $A\lambda$ is the absorbance of the probe at the excitation wavelength (more specifically, at 785 and 808 nm). A more detailed description of the calculation process is explained in the ESI.†

The photothermal conversion efficiencies of all samples are presented in Table 4. G-NH$_2$ and AuBPs exposed to 785 nm excitation wavelength exhibit η = 41% and η = 74%, respectively. However, the hybrid nanosystem consisting of both G-NH$_2$ and AuBPs, G–PMA(1:1)/(1:3)@AuBPs exhibit η = 62% and η = 75% when exposed to the 785 nm laser. Nevertheless, even though G-NH$_2$ and AuBPs exhibit lower η, 34% and 43%, respectively when exposed to the 808 nm laser, the hybrid nanosystems possess an increased photothermal conversion efficiency coefficient, with η = 71% for G–PMA(1:1)@AuBPs and η = 75% for G–PMA(1:3)@AuBPs.

As observed in Table 4, G–PMA(1:3)@AuBPs remains consistent under both 785 and 808 nm irradiation; however, the higher ΔT_{max} value observed at 808 nm is attributed to: (i) the stronger absorption of AuBPs at this specific wavelength, thus enhancing heat generation, and (ii) the higher incident laser power (0.29 W over 0.17 W for 785 nm), leading to greater energy input.

The photothermal performance of the hybrid nanosystems is significantly enhanced compared to one of the starting materials, providing the efficiency of our strategy to combine appropriately two PTAs, reaching a hybrid nanocomposite endowed with promising thermoplasmonic properties.

In vitro cytotoxicity evaluation

The cytotoxicity of G–PMA(1:1)/(1:3) and G–PMA(1:1)/(1:3)@AuBPs was evaluated on melanoma B16F10 cells with different amounts of samples (from 0 to 40 μL of a dispersion 0.3 mg mL^{-1} in PBS) (Fig. S7, ESI†).

Graphs and statistical analysis were performed with Graph-Pad Prism 9 software. Statistical differences were analyzed for each treatment compared to control cells with the "repeated measures ANOVA" test followed by "Dunnett's multiple comparison test" with the setting of p-value <0.001 ***. G–PMA induced an inhibition of cell growth between 37–20%. In contrast, G–PMA@Au systems proved slightly more cytotoxic at higher doses with a growth inhibition from 46% to 20%.

A comparison using the two-way ANOVA test between G–PMA(1:1) *vs.* G–PMA(1:3) and G–PMA(1:1)@AuPBS *vs.* G–PMA(1:3)@AuPBS did not identify statistically significant differences between samples. G–PMA(1:1)@AuBPs and G–PMA(1:3)@AuBPs

4442 | *J. Mater. Chem. B*, 2025, **13**, 4433–4446

This journal is © The Royal Society of Chemistry 2025

exhibit similar behaviors, with a notable decrease in viability only at the higher tested volumes (Fig. S7, ESI†). However, in both cases, no significant cytotoxic effect on the B16F10 melanoma cells was observed, assessing their potentiality for biomedical applications, even at the highest tested concentrations.

In vitro cell imaging

To initially assess the internalization and localization of the G–PMA@AuBP nanosystem, conventional fluorescence combined with dark-field microscopy of the treated cells was employed as a powerful tool for imaging plasmonic NPs within B16F10 melanoma cells, by recording the scattering of the AuBPs. The capability of the AuBPs to effectively scatter light facilitated the detection of the nanosystem's internalization. The image of treated cells, presented in Fig. 7B, reveals luminous spots within their cytoplasm and surrounding the nucleus, which was fluorescently stained with DAPI, confirming the presence of the nanocomposite inside the cells. This demonstrates the ability of G–PMA(1:1)@AuBPs to act as a scattering contrast

agent. In contrast, the control image (Fig. 7A) reveals no bright spots within the cytoplasm of the untreated B16F10 cells.

The intracellular fate of G–PMA(1:1)@AuBPs in B16F10 melanoma cells has been investigated also by FLIM, an ideal tool to assess changes in the local microenvironment in the proximity of the fluorescent molecules inside the cell.[46] Exploiting the confocal FLIM technique, we evaluated the intrinsic autofluorescence property of the G–PMA(1:1)@AuBP hybrid nanosystem, confirming the ability of G–PMA(1:1)@AuBPs to behave as *in vitro* label-free fluorescent contrast agents. Thus, FLIM was conducted under 520 nm excitation. The fluorescence lifetime maps depicted in Fig. 8 substantiate the heightened cellular uptake of G–PMA(1:1)@AuBPs. Moreover, these images captured at varying depths within the cell reveal the presence of uniformly distributed fluorescence signals. The fluorescence signal observed in the cytoplasm exhibits an average lifetime of 2.8 ns, whereas the fluorescence observed inside the nuclei, is assumed to arise from the small-sized G sheets able to penetrate the nuclear membrane, as previously observed,[1] has a lifetime of 3.25 ns (Fig. S8, ESI†). Comparing
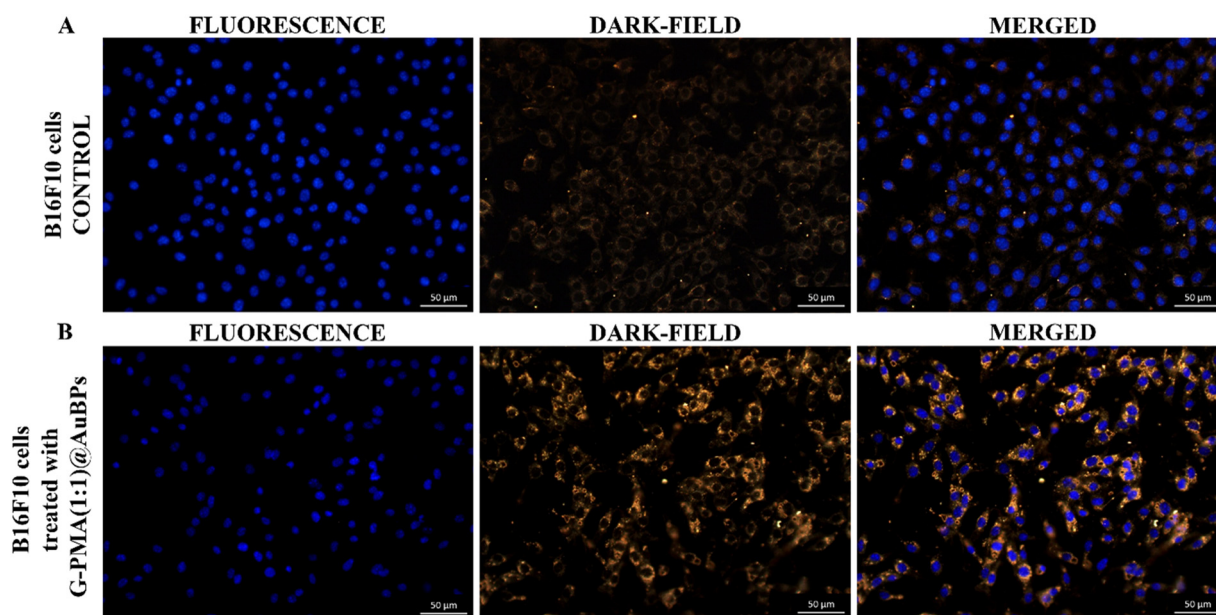

Fig. 7 Conventional fluorescence and dark-field images of the (A) control B16F10 melanoma cells and (B) B16F10 melanoma cells treated with G–PMA(1:1)@AuBPs. For fluorescence images, the nuclei of the cells were stained with DAPI (blue emission).
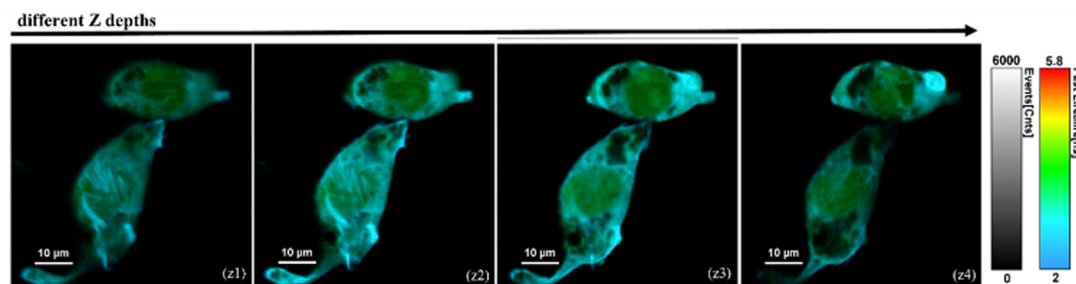

Fig. 8 FLIM images of the B16F10 melanoma cells treated with G–PMA(1:1)@AuBPs at different z-depths, under excitation at 520 nm.

This journal is © The Royal Society of Chemistry 2025

J. Mater. Chem. B, 2025, **13**, 4433–4446 | **4443**

the FLIM images of the untreated (Fig. S7, ESI†) with treated cells (Fig. 8), it is clear that the G–PMA(1 : 1)@AuBP nanosystem is localized inside the cells, in the cytoplasm, and that the fluorescence presented in Fig. 8 is due to the presence of G–PMA(1 : 1)@AuBPs in the cytoplasm. These findings corroborate the consistent internalization and the effective cellular staining achieved, thereby demonstrating the potential of the hybrid G–PMA(1 : 1)@AuBP nanosystem as an effective label-free fluorescent contrast agent for intracellular imaging.

In vitro NIR irradiation assay

To assess the efficiency of the G–PMA@AuBP nanosystems in acting as PTAs *in vitro*, B16F10 melanoma cells were treated with both nanocomposites—G–PMA(1 : 1)@AuBPs and G–PMA(1 : 3)@AuBPs—and exposed to 15 min of irradiation with the 808 nm continuous laser (Fig. 9). The non-irradiated cells treated under the same conditions were used as a control. As expected, the viability of non-irradiated cells was lower than reported in Fig. S9 (ESI†) due to the stressed experimental conditions adopted during the irradiation assay.

NIR treatment significantly affected the cell viability in comparison with the non-irradiated cells cultured under the same experimental conditions. Cells irradiated and treated with G–PMA(1 : 1)@AuPBs induced an enhanced cytotoxic effect with growth inhibition between 61 and 90%, and G–PMA(1 : 3)@AuPBs have proved slightly more cytotoxic at higher doses with growth inhibition from 24% to 93%, compared with irradiated control cells. A comparison using the two-way ANOVA test between G–PMA(1 : 1)@AuPBs *vs.* irradiated G–PMA(1 : 1)@AuPBs showed statistically highly significant differences between samples treated with small volumes, and for G–PMA(1 : 3)@AuPBs *vs.* irradiated G–PMA(1 : 3)@AuPBs a difference was observed only for 4 and 5 μL volumes (in the graphics, the results for two-way ANOVA analysis appear with a brace with red stars) (Fig. 9).

The present results, together with the good biocompatibility previously discussed, highlight the potentiality of such nanohybrid systems for PTT applications. Taken together, G–PMA(1 : 1)@AuPBs

at low doses, with good biocompatibility, appear to be more effective than G–PMA(1 : 3)@AuPBs, especially in terms of response to irradiation.

The applicability in targeting and killing tumor cells can be improved by conjugation with tumor-targeting compounds. The new NIR irradiation technologies can adjust the radiation beam with a preponderance on the tumor area so that the surrounding normal cells can be protected. Furthermore, comparative *in vitro* studies of these nano-systems on normal cells could elucidate if there is a selectivity of uptake by tumor cells. Also, initiating *in vivo* studies with these therapies could show the effects of these nano-systems on both the tumor micro-environment and implicitly on immune system cells as well as the vascular effects associated with the therapy.

Conclusions

In this work, we developed and described the peculiar properties of two new hybrid nanosystems (G–PMA(1 : 1)@AuBPs, G–PMA-(1 : 3)@AuBPs) based on the combination of amine-graphene (G-NH$_2$), PMA and Au bipyramids. The obtained nanocomposites behave simultaneously like NIR-responsive platforms for photo-thermal therapy applications and efficient contrast agents for bioimaging. The nanosystems were obtained by covalent and supramolecular approaches, while their structure, chemical composition, and morphology were investigated by Raman spectroscopy, XPS, XRD, and STEM analysis.

G–PMA@AuBPs present a great light-to-heat conversion efficiency when exposed to NIR light (specifically 785 and 808 nm), particularly the systems showed a photothermal conversion efficiency coefficient (η) over 70% when irradiated at 808 nm, a value significantly higher compared to the ones of the starting materials. Furthermore, the *in vitro* phototherapeutic effect of the as-developed G–PMA@AuBP nanosystems under 808 nm laser exposure was assessed, proving promising results against melanoma cells *via* photothermal therapy.
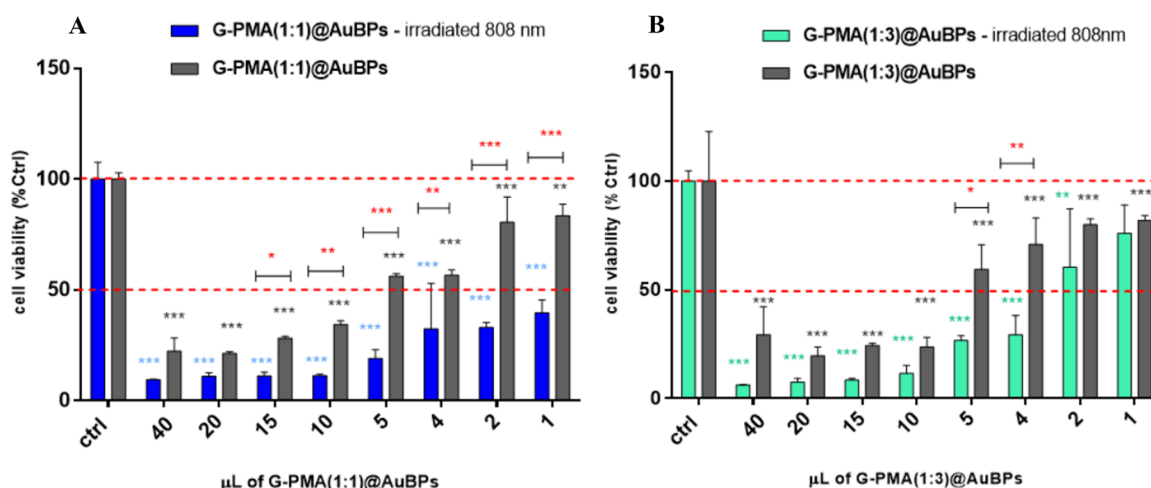

Fig. 9 MTT cell assay of B16F10 melanoma cells (A) after treatment with G–PMA(1 : 1)@AuBPs (gray) and after 15 min irradiation with a 808 nm laser (blue); (B) after treatment with G–PMA(1 : 3)@AuBPs (gray) and after 15 min irradiation with a 808 nm laser (green).

4444 | *J. Mater. Chem. B*, 2025, **13**, 4433–4446

This journal is © The Royal Society of Chemistry 2025

The capacity of nanohybrid systems to function as an effective label-free contrast agent, allowing for straightforward tracking within B16F10 melanoma cells, was validated by using conventional fluorescence, dark-field microscopy, and FLIM techniques.

Overall, the current study points to the relevance of well-thought-out nanohybrid systems, which not only integrate the features of each component but also generate new properties due to the synergistic interaction of starting materials. The G–PMA@AuBP nanocomposite is a promising theranostic nanomedicine tool able to exert simultaneously in vivo fluorescence imaging as well as PTT effects for cancer treatment. The preparation of such nanohybrid PTA reveals advantageous properties combining the phototherapeutic activity of AuBPs with the high NIR absorbance and fluorescent contrast agent ability of G-NH$_2$[30] and helps in overcoming the drawbacks relative to the poor biocompatibility and colloidal stability of G-NH$_2$ through covalent derivatization with PMA.

Author contributions

Conceptualization: Anna Piperno and Giulia Neri; investigation: Daria Stoia, Monica Focsan and Giulia Neri; formal analysis: Daria Stoia, Enza Fazio, Carmelo Corsaro, Olga Soritau, Gabriela Chereches, Monica Focsan, Ana Maria Craciun; supervision: Giulia Neri and Monica Focsan; writing – original draft: Daria Stoia and Giulia Neri; writing – review and editing: all authors. Funding acquisition: Monica Focsan. All authors have read and agreed to the published version of the manuscript.

Data availability

The data supporting this article have been included as part of the ESI.†

Conflicts of interest

There are no conflicts to declare.

Acknowledgements

References

1 H. Hou, L. Cardo, J. P. Merino, F. Xu, C. Wetzl, B. Arnaiz, X. Luan, Y. Mai, A. Criado and M. Prato, *Mater. Today Chem.*, 2023, **33**, 101668.

2 J. Li, W. Zhang, W. Ji, J. Wang, N. Wang, W. Wu, Q. Wu, X. Hou, W. Hu and L. Li, *J. Mater. Chem. B*, 2021, **9**, 7909–7926.

3 W. Bian, Y. Wang, Z. Pan, N. Chen, X. Li, W.-L. Wong, X. Liu, Y. He, K. Zhang and Y.-J. Lu, *ACS Appl. Nano Mater.*, 2021, **4**, 11353–11385.

4 B. Liu, F. Jiang, J. Sun, F. Wang and K. Liu, *J. Mater. Chem. B*, 2021, **9**, 7007–7022.

5 V. P. Pattani, J. Shah, A. Atalis, A. Sharma and J. W. Tunnell, *J. Nanopart. Res.*, 2015, **17**, 20.

6 L. Tong, Y. Zhao, T. B. Huff, M. N. Hansen, A. Wei and J.-X. Cheng, *Adv. Mater.*, 2007, **19**, 3136–3141.

7 X. Ai, J. Mu and B. Xing, *Theranostics*, 2016, **6**, 2439–2457.

8 D. F. Báez, *Pharmaceutics*, 2023, **15**, 2286.

9 M. F. Naief, S. N. Mohammed, H. J. Mayouf and A. M. Mohammed, *J. Organomet. Chem.*, 2023, **999**, 122819.

10 W. Mei, S. Yao, X. Cai, Q. Xu, H. Hu, Z. Xu and X. Dai, *J. Mater. Chem. B*, 2025, **13**, 1781–1793.

11 Y. Hu, B. Y. Zhang, F. Haque, G. Ren and J. Z. Ou, *Mater. Horiz.*, 2022, **9**, 2288–2324.

12 X. Qi, Y. Xiang, E. Cai, X. Ge, X. Chen, W. Zhang, Z. Li and J. Shen, *Coord. Chem. Rev.*, 2023, **496**, 215426.

13 Y.-W. Chen, Y.-L. Su, S.-H. Hu and S.-Y. Chen, *Adv. Drug Delivery Rev.*, 2016, **105**, 190–204.

14 D. de Melo-Diogo, R. Lima-Sousa, C. G. Alves and I. J. Correia, *Biomater. Sci.*, 2019, **7**, 3534–3551.

15 R. Li, C. Liu, C. Wan, T. Liu, R. Zhang, J. Du, X. Wang, X. Jiao, R. Gao and B. Li, *Int. J. Nanomed.*, 2023, **18**, 3309–3324.

16 L. A. Al-Ani, M. A. AlSaadi, F. A. Kadir, N. M. Hashim, N. M. Julkapli and W. A. Yehye, *Eur. J. Med. Chem.*, 2017, **139**, 349–366.

17 A. Campu, M. Focsan, F. Lerouge, R. Borlan, L. Tie, D. Rugina and S. Astilean, *Colloids Surf., B*, 2020, **194**, 111213.

18 M. Wu, Y. Xiao, R. Wu, J. Lei, T. Li and Y. Zheng, *J. Mater. Chem. B*, 2024, **12**, 8048–8061.

19 Y. Xu, X. Wang, L. Cheng, Z. Liu and Q. Zhang, *Chem. Eng. J.*, 2019, **378**, 122025.

20 Q. Yu, Y. Han, X. Wang, C. Qin, D. Zhai, Z. Yi, J. Chang, Y. Xiao and C. Wu, *ACS Nano*, 2018, **12**, 2695–2707.

21 Z. Sobhani, M. A. Behnam, F. Emami, A. Dehghanian and I. Jamhiri, *Int. J. Nanomed.*, 2017, **12**, 4509–4517.

22 B.-P. Jiang, L. Zhang, X.-L. Guo, X.-C. Shen, Y. Wang, Y. Zhu and H. Liang, *Small*, 2017, **13**, 1602496.

23 R. Mendes, P. Pedrosa, J. C. Lima, A. R. Fernandes and P. V. Baptista, *Sci. Rep.*, 2017, **7**, 10872.

24 A. S. Bear, L. C. Kennedy, J. K. Young, S. K. Perna, J. P. Mattos Almeida, A. Y. Lin, P. C. Eckels, R. A. Drezek and A. E. Foster, *PLoS One*, 2013, **8**, e69073.

25 S. Parida, C. Maiti, Y. Rajesh, K. K. Dey, I. Pal, A. Parekh, R. Patra, D. Dhara, P. K. Dutta and M. Mandal, *Biochim. Biophys. Acta, Gen. Subj.*, 2017, **1861**, 3039–3052.

26 X. Liu, W. Zhou, T. Wang, S. Miao, S. Lan, Z. Wei, Z. Meng, Q. Dai and H. Fan, *Sci. Rep.*, 2023, **13**, 3372.

27 M. Z. Iqbal, M. S. Katsiotis, S. M. Alhassan, M. W. Liberatore and A. A. Abdala, *RSC Adv.*, 2014, **4**, 6830–6839.

28 D. Chateau, A. Liotta, F. Vadcard, J. R. G. Navarro, F. Chaput, J. Lermé, F. Lerouge and S. Parola, *Nanoscale*, 2015, **7**, 1934–1943.

This journal is © The Royal Society of Chemistry 2025

J. Mater. Chem. B, 2025, **13**, 4433–4446 | **4445**

29 A. Campu, A.-M. Craciun, M. Focsan and S. Astilean, *Nanotechnology*, 2019, **30**, 405701.

30 P. Zheng and N. Wu, *Chem. – Asian J.*, 2017, **12**, 2343–2353.

31 C. Corsaro, G. Neri, A. Santoro and E. Fazio, *Materials*, 2022, **15**, 282.

32 M. Liu and P. Guyot-Sionnest, *J. Phys. Chem. B*, 2005, **109**, 22192–22200.

33 F. Hubert, F. Testard and O. Spalla, *Langmuir*, 2008, **24**, 9219–9222.

34 N. R. Jana, L. Gearheart and C. J. Murphy, *Adv. Mater.*, 2001, **13**, 1389–1393.

35 C. J. Murphy, L. B. Thompson, D. J. Chernak, J. A. Yang, S. T. Sivapalan, S. P. Boulos, J. Huang, A. M. Alkilany and P. N. Sisco, *Curr. Opin. Colloid Interface Sci.*, 2011, **16**, 128–134.

36 M. A. Pimenta, G. Dresselhaus, M. S. Dresselhaus, L. G. Cançado, A. Jorio and R. Saito, *Phys. Chem. Chem. Phys.*, 2007, **9**, 1276–1290.

37 S. Stankovich, D. A. Dikin, R. D. Piner, K. A. Kohlhaas, A. Kleinhammes, Y. Jia, Y. Wu, S. T. Nguyen and R. S. Ruoff, *Carbon*, 2007, **45**, 1558–1565.

38 G. Neri, A. Scala, F. Barreca, E. Fazio, P. G. Mineo, A. Mazzaglia, G. Grassi and A. Piperno, *Chem. Commun.*, 2015, **51**, 4846–4849.

39 M. U. Amin, R. Zhang, L. Li, H. You and J. Fang, *Anal. Chem.*, 2021, **93**, 7657–7664.

40 A. R. Biris, S. Pruneanu, F. Pogacean, M. D. Lazar, G. Borodi, S. Ardelean, E. Dervishi, F. Watanabe and A. S. Biris, *Int. J. Nanomed.*, 2013, **8**, 1429–1438.

41 S. Krishnamurthy, A. Esterle, N. C. Sharma and S. V. Sahi, *Nanoscale Res. Lett.*, 2014, **9**, 627.

42 G. Hannon, F. L. Tansi, I. Hilger and A. Prina-Mello, *Adv. Ther.*, 2021, **4**, 2000267.

43 G. Camille, M. Albert, S. Aurelie, M. Serge and F. Celine, *Curr. Med. Chem.*, 2014, **21**, 1871–1897.

44 C. L. West, A. C. V. Doughty, K. Liu and W. R. Chen, *J. Bio-X Res.*, 2019, **02**, 159–168.

45 D. Stoia, R. Pop, A. Campu, M. Nistor, S. Astilean, A. Pintea, M. Suciu, D. Rugina and M. Focsan, *Colloids Surf., B*, 2022, **220**, 112915.

46 A. Piperno, A. Mazzaglia, A. Scala, R. Pennisi, R. Zagami, G. Neri, S. M. Torcasio, C. Rosmini, P. G. Mineo, M. Potara, M. Focsan, S. Astilean, G. G. Zhou and M. T. Sciortino, *ACS Appl. Mater. Interfaces*, 2019, **11**, 46101–46111.

4446 | *J. Mater. Chem. B*, 2025, **13**, 4433–4446

This journal is © The Royal Society of Chemistry 2025